INT. J. REMOTE SENSING, 1998, VOL. 19, NO. 6, 1147–1160

Exploring the utility potential of SAR interferometric coherence images

C. ICHOKU, A. KARNIELI

Jacob Blaustein Institute for Desert Research, Ben-Gurion University of the Negev, Sede-Boker Campus 84990, Israel

Y. ARKIN

Geological Survey of Israel, 30 Malchei Yisrael Street, Jerusalem 95501, Israel

J. CHOROWICZ, T. FLEURY and J-P. RUDANT

Laboratoire de Géologie-Géomorphologie Structurale et Télédétection, Université Pierre et Marie Curie, 4 Place Jussieu, 75252 Paris 05, France

(*Received 6 February 1997; in final form 19 August 1997*)

Abstract. Using interferometric techniques, a complex coherence image was generated from a pair of complex SAR data. Amplitude images were computed from the SAR and coherence images and subjected to Principal Components Analysis. The first channel of this analysis is an image of remarkable clarity and detail, suitable for various applications. A good lithologic interpretation was realized from this single image channel alone.

1. Introduction

Synthetic Aperture Radar (SAR) is generally known to possess a number of advantages over visible/infrared systems. These include its all-weather, day and night image acquisition capability unhindered by cloud cover; its potential to express surface roughness prominently; and its ability to penetrate the soil in certain cases. However, unlike multi-spectral visible/infrared imagery, radar images often consist of only a single channel which is often contaminated by speckle—a type of grainy effect resulting from phase variations of radar waves from unit reflectors within a resolution cell. This has imposed serious limitations on the interpretability of radar imagery, thereby hampering its use as an independent viable data source. Consequently, a great deal of research effort has been devoted to integrating radar imagery with other types of data (mostly visible/infrared images of the type acquired by Landsat and SPOT) (e.g., Schistad *et al.* 1994, and Saint-Jean *et al.* 1995).

Several efforts have been made by researchers to improve the visual quality and indeed the general utility of SAR imagery. To this effect, several techniques have been developed and applied. These include multi-look processing (Lee *et al.* 1994 a, Rudant *et al.* 1994), speckle filtering (Safa and Flouzat 1989, Lee *et al.* 1994 b), and textural analysis (Henebry and Kux 1995, Beauchemin *et al.* 1996). Even these processes do not improve radar images significantly.

One SAR based technique which has generated considerable interest among remote sensing scientists and users is interferometry (Massonnet and Rabaute 1993, Zebker *et al.* 1994, Gens and Van Genderen 1996). This technique involves the use

of pairs of complex SAR images which contain both amplitude and phase information. It is this composite quality of the images that enables interferometry whose main product is interferogram which is also a complex image. The phase component of the interferogram (which shows the now almost familiar interferometric fringes) is the phase difference between the input complex SAR image pair. Nevertheless, complex coherence images representing the phase correlation between the interferometric pair can also be generated from them as a by-product of this technique.

Great emphasis has thus far been laid on the applicability of interferograms. Some of the current applications include the generation of Digital Elevation Models (Zebker *et al.* 1994), detection of terrain displacements (Massonnet *et al.* 1993), monitoring of ice sheet motions (Goldstein *et al.* 1993), measuring ocean surface currents (Goldstein and Zebker 1987, Goldstein *et al.* 1989), and so on. On the other hand, coherence images are merely regarded as a means of verifying phase coherence. They are usually not considered as very useful images in themselves. In the few cases where the utility of the coherence image has been discussed (e.g., Wegmuller *et al.* 1995), mostly its obvious relevance to change detection is highlighted, ignoring its other more subtle potentialities. Even when other applications have been treated, most workers have sought to interpret and extract information directly from the coherence images alone without further processing (Askne and Hagberg 1993, D'Iorio *et al.* 1996). In this paper, we demonstrate how incredibly simple image processing operations can transform coherence images (in combination with ordinary SAR images) into formidable information-bearing images of striking geologic importance.

2. Study area

We are currently doing a study on the application of radar imagery to the mapping of geology, geomorphology, and risks related to active faults and associated seismic activity in the Dead Sea Rift Valley section of the major Syro-African Rift System. However, for detailed analysis, illustration, and interferometry, we have chosen, from the Jordan Valley segment of the rift, a study area measuring about 36 km (north–south) by 28 km (east–west). This area is centred approximately at latitude 32°06′N and Longitude 35°32′E between the Sea of Galilee and the Dead Sea (see figure 1). Figure 1 shows the geological map of the study area extracted from the 1/500 000 scale geological photomap of Israel (Bartov and Arkin 1979).

The study area has a number of interesting geomorphostructural characteristics. Topographically, it is made up of three distinct levels. The top level corresponds to the regional topography and geology, with Mesozoic carbonates and clastics forming the mountainous shoulders of the rift. Below this is the rift floor, with alluvial fans and other deposits, as well as the Plio-Pleistocene Lisan formation comprising chalk, marl, and conglomerates. The third level is the bottom of the valley cutting through the rift floor. This is the flood plain of the present day Jordan River with typical Quaternary to Holocene deposits of alluviums and conglomerates. The Jordan River itself meanders through the third level. Another remarkable feature of the study area is that, here, north–west to west trending splays depart from the general north–south strike of the Rift and continue up to as far as the Mediterranean Sea. The morphostructural features described here can be appreciated on figure 2 which is a shaded relief image generated from the Digital Elevation Model (DEM) of the study area extracted from the Digital Terrain Map of Israel described in Hall (1993).

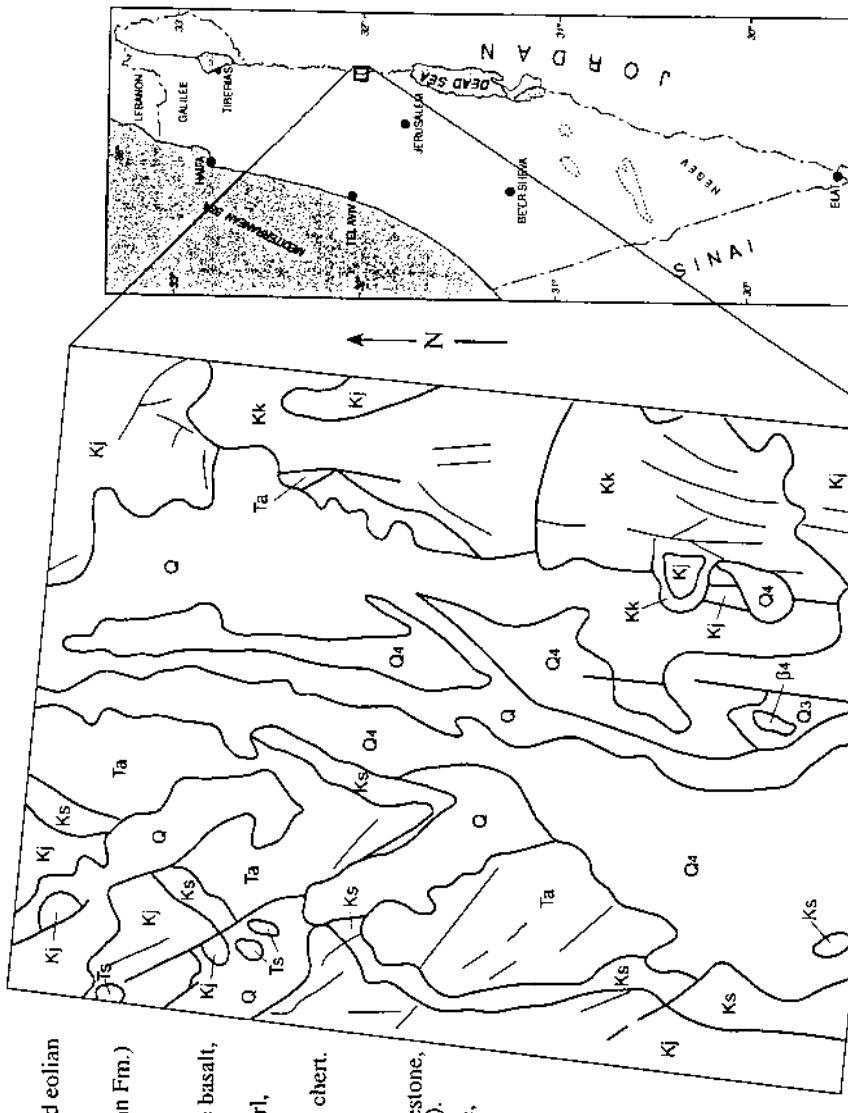

Figure 1. Geological map of the study area extracted from the 1/500 000 scale geological photomap of Israel.

Figure 2. Shaded relief Digital Elevation Model (DEM) of the study area (illumination direction: Azimuth = 270°, Altitude = 45°).

3. Overview of interferometric data and techniques, and coherence image generation

SAR interferometry involves the use of a pair of complex images (which contain amplitude and phase information), acquired from two close (almost repeat) orbits, to generate an interferogram. The quality of an interferogram is largely determined by the level of correlation between the two complex images used to create it. The various sources of decorrelation and possible remedies were discussed by Zebker

and Villasenor (1992), and Bamler and Just (1993). They include thermal, spatial, and temporal decorrelations. Whereas thermal decorrelation is due to radar sensor noise, spatial decorrelation is related to the baseline, while temporal decorrelation depends on changes in the scene (which is often a function of the time interval between the acquisition of the two images). The effect of thermal decorrelation can be reduced by modelling, and it is relatively easy to optimize spatial and temporal correlations from the user standpoint by choosing images having a convenient baseline and acquired over a short time interval.

In this study, we used a pair of Single Look Complex (SLC) images of the ERS1-SAR which is a *C*-band (5·66 cm wavelength), *VV* polarized radar operating from an altitude of 785 km with a mean look angle of 23°. Our images were acquired on 1 and 13 January 1994 (12 day interval) from orbits 12 877 and 13 049 respectively, and they belong to frame number 2961. The baseline component perpendicular to the look direction is 183 m. The SLC images have a pixel spacing of about 3·9 m in azimuth and 7·9 m in slant range. We used a pair of sub-images each measuring 8000 pixels in azimuth by 1000 pixels in range.

Interferometry was carried out using the ISAR software developed by the European Space Agency (ESA) in the framework of the Fringe Working Group (Coulson and Solaas 1993). The procedure employs the basic principles of interferometry as described by Massonnet and Rabaute (1993), Zebker *et al.* (1994), Vachon *et al.* (1995), and Gens and Van Genderen (1996), among others. An interferogram is computed from a coregistered pair of complex SAR images as follows:

$$p(x,y) = z_1(x,y)\bar{z}_2^*(x,y) \tag{1}$$

where $p(x,y)$ represents the complex interferogram value at pixel (x,y), $z_1(x,y)$ is the complex value at pixel (x,y) of one SAR image, $\bar{z}_2^*(x,y)$ is the complex conjugate of the corresponding pixel (x,y) value of the other image.

Coherence, which is a measure of phase correlation, is defined as the correlation coefficient:

$$g(x,y) = \frac{E[z_1(x,y)\bar{z}_2^*(x,y)]}{\sqrt{(E[|z_1(x,y)|^2]E[|z_2(x,y)|^2])}} \tag{2}$$

where $g(x,y)$ is the value of coherence at pixel (x,y), $z_1(x,y)$ and $z_2(x,y)$ are as defined above, while $E[\ ]$ designates mathematical expectation.

In practice, coherence is computed from:

$$g(x,y) = \frac{\langle z_1(x,y)\bar{z}_2^*(x,y)\rangle}{\sqrt{(\langle|z_1(x,y)|^2\rangle\langle|z_2(x,y)|^2\rangle)}} \tag{3}$$

where $\langle\ \rangle$ denotes spatial averaging over a processing window centred on pixel (x,y); and the other parameters are as previously defined.

In this work, both the interferogram and coherence were generated and averaged 10 pixels in azimuth and 2 pixels in range to produce 10-look images representing ground elements measuring about 50 m × 50 m (Massonnet and Rabaute 1993, Zebker *et al.* 1994). We also performed the same operation on the SLC images to bring them to the same resolution to facilitate the subsequent combined image processing.

4. Image processing

Like the original SLC data, both the interferogram and the coherence are complex images. Each can be decomposed into its amplitude and phase components. Usually, it is these components that are used for intelligible visual displays: the phase component for the interferogram and the amplitude component for others (SLC and coherence).

We computed the amplitude images of the SLC and coherence, and applied a linear contrast stretch to each of them. The amplitude of the SLC data is what is generally known as the SAR image; thus, henceforth, we shall simply refer to it as the SAR image. Similarly, the amplitude of the coherence will be referred to as coherence image. We performed several simple multi-band image processing operations (including image arithmetic, filtering, and image transformations) using the SAR and the coherence images, and obtained different results that range from poor to good, based on visual assessment. One of the main operations performed was the Principal Components Analysis (PCA) between one of the SAR images and the Coherence image. The first channel of this analysis (which we shall call PCA1SC: denoting PCA channel 1 between the SAR and Coherence images) is quite impressive. This is the main result presented here. The PCA was performed using the PCI image processing software package, though it is possible with most other similar packages. It is pertinent to mention that the first channel of a PCA operation (such as the PCA1SC) expresses the combined maximum variability between the input images (Mather 1987, p. 208). This is because PCA is a statistical transformation which rotates the axes of a multi-dimensional image space (as represented in a multi-band scatterplot) in such a way that they lie in the direction of maximum data variance (i.e. pixel values are expressed with respect to the principal axes of the ellipse or ellipsoid enclosing the scatter of points instead of the original axes representing the individual bands). Thus, the first principal component (in our case the PCA1SC) represents the longest of the new axes and contains the largest amount of variability information from the input channels (which in this case are the SAR and coherence images).

After the various image processing stages, all the images presented in this work were geocoded and registered to the DEM which is itself tied to the ground coordinate system. This is to enable detailed comparative analysis. Figures 3, 4, and 5 show respectively the geocoded SAR image, coherence image, and PCA1SC.

5. Analysis of result

We shall evaluate the result of this work (the PCA1SC shown in figure 5) by comparing it with the SAR and coherence images (figures 3 and 4) as well as a Landsat-TM false-colour composite (RGB = bands 4-3-2) shown in figure 6. From the geological point of view, the PCA1SC (figure 5) seems to possess all the advantages derivable from all the other images put together, and at the same time appears to be free of their disadvantages. Like the SAR image (figure 3), it portrays surface morphology prominently, but in a more natural form (almost like the relief shaded DEM in figure 2). For instance, the layover areas appear dark rather than bright, thereby making the PCA1SC look more intelligible even to the non specialist. However, this reverse tonal effect is not a peculiar outcome of the PCA process, as it can also result from a negative of the SAR image. Another appreciable attribute of the PCA1SC is that, unlike the SAR image and like the Landsat-TM (figure 6), it expresses vegetated areas very clearly, and in fact, they are almost as well expressed

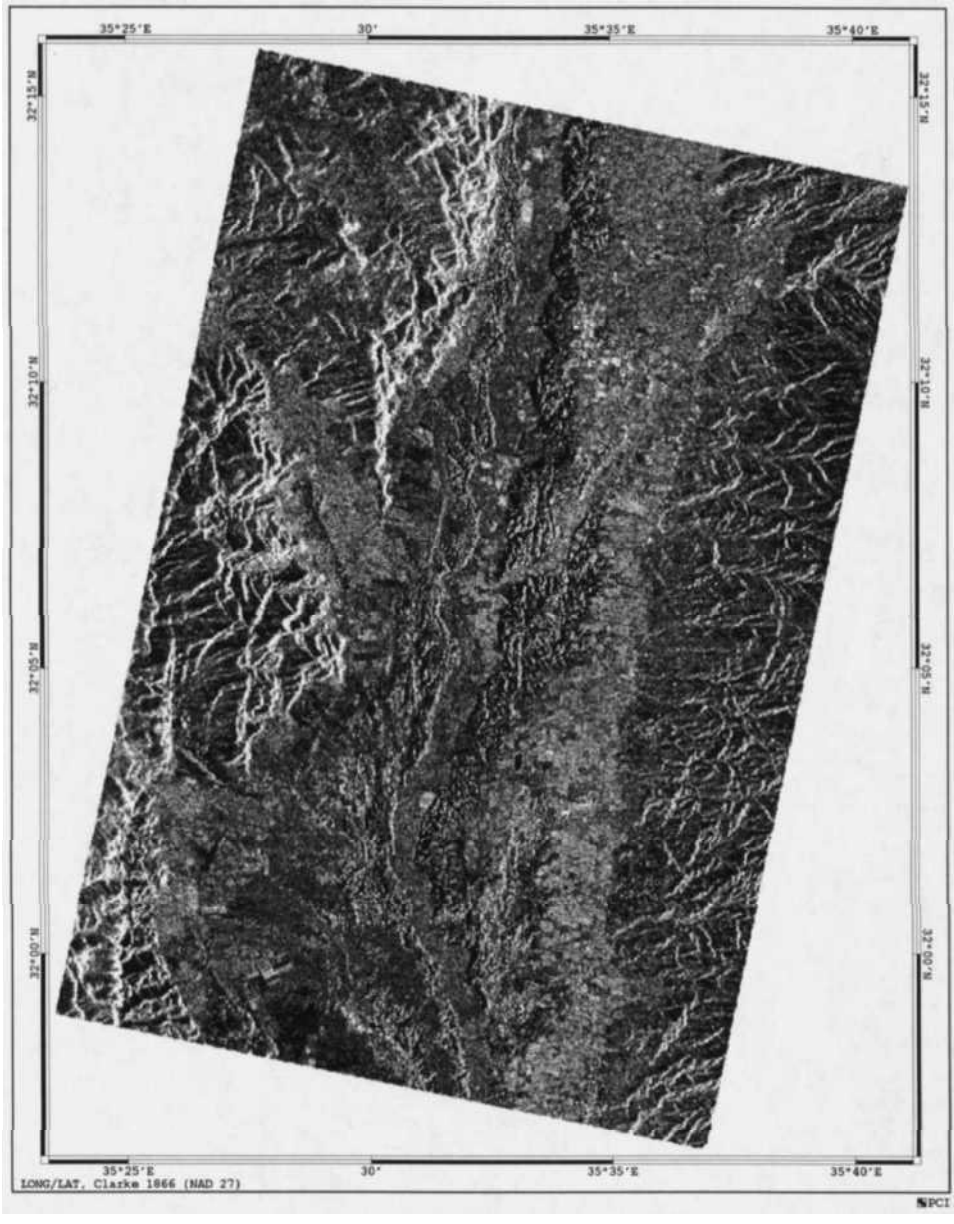

Figure 3. Geocoded (10-look) amplitude image generated from the SLC data of 1 January 1994.

as in aerial photographs of similar scales. Since differences in vegetation characteristics are often an expression of lithological differences, lithological boundaries are very distinct. Also, certain other geologic features are more prominent.

To demonstrate the geological utility of the PCA1SC image in real terms, we performed a manual interpretation and delineation of lithological boundaries on it. The result of our interpretation process is shown in figure 7. The topomorphologic levels described in § 2 are clearly distinguishable, and the letters *A*, *B*, and *C* have

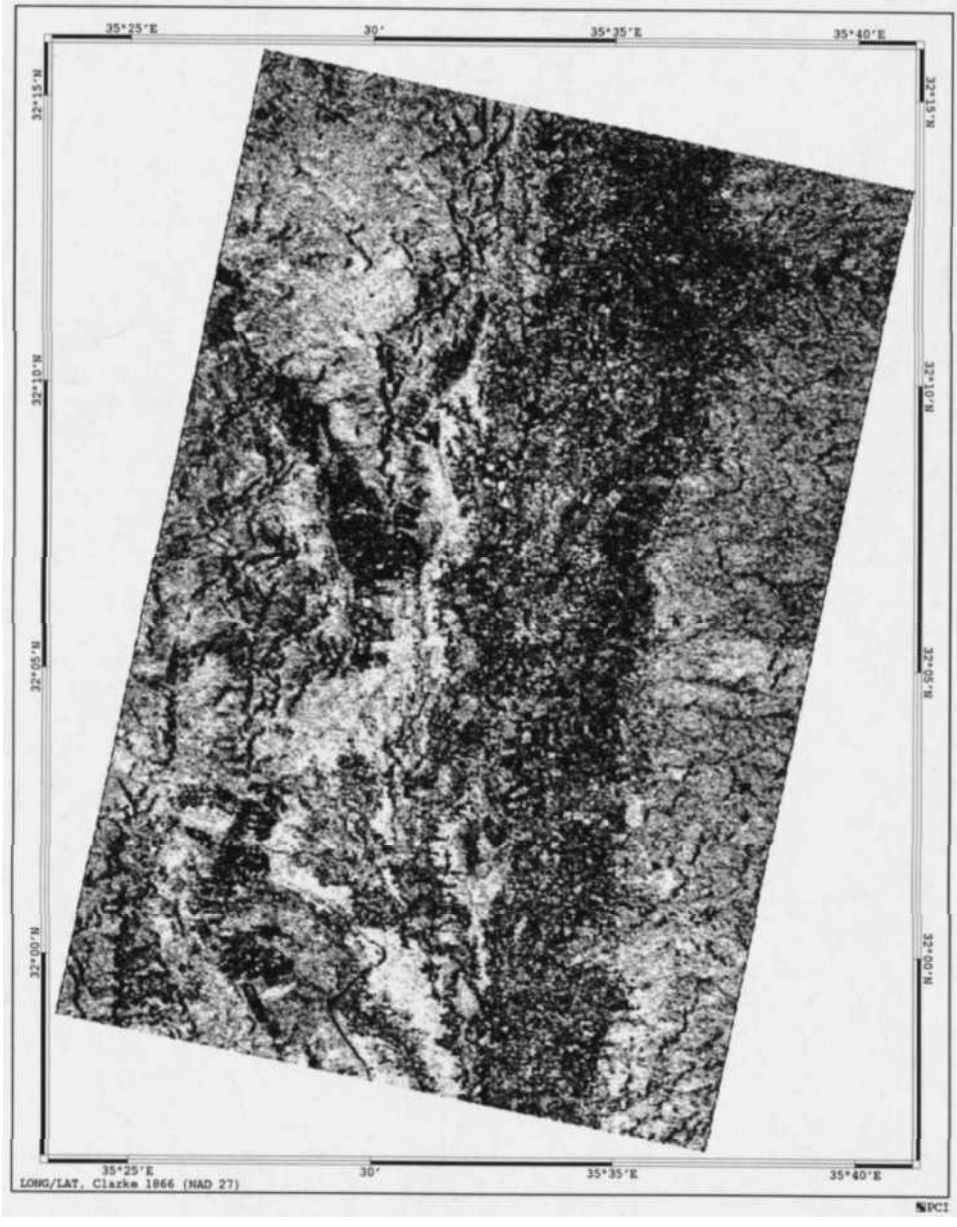

Figure 4. Geocoded (10-look) amplitude image generated from the complex coherence image.

been used to designate the top, middle, and bottom levels respectively, while the numeric suffixes (1, 2, 3, ...) are used to identify the different units in each level. The rift shoulders were previously well mapped, so, we have had no need to do a detailed interpretation here. However, within the area covered by our images each shoulder has a more-or-less homogeneous lithology, and we have designated the West and East sides by A1 and A2 respectively. We concentrated on the rift floor (level B) whose original lithological mapping was relatively poor. The attention of the reader is drawn to the lithological diversity expressed here. Not only is the Lisan formation

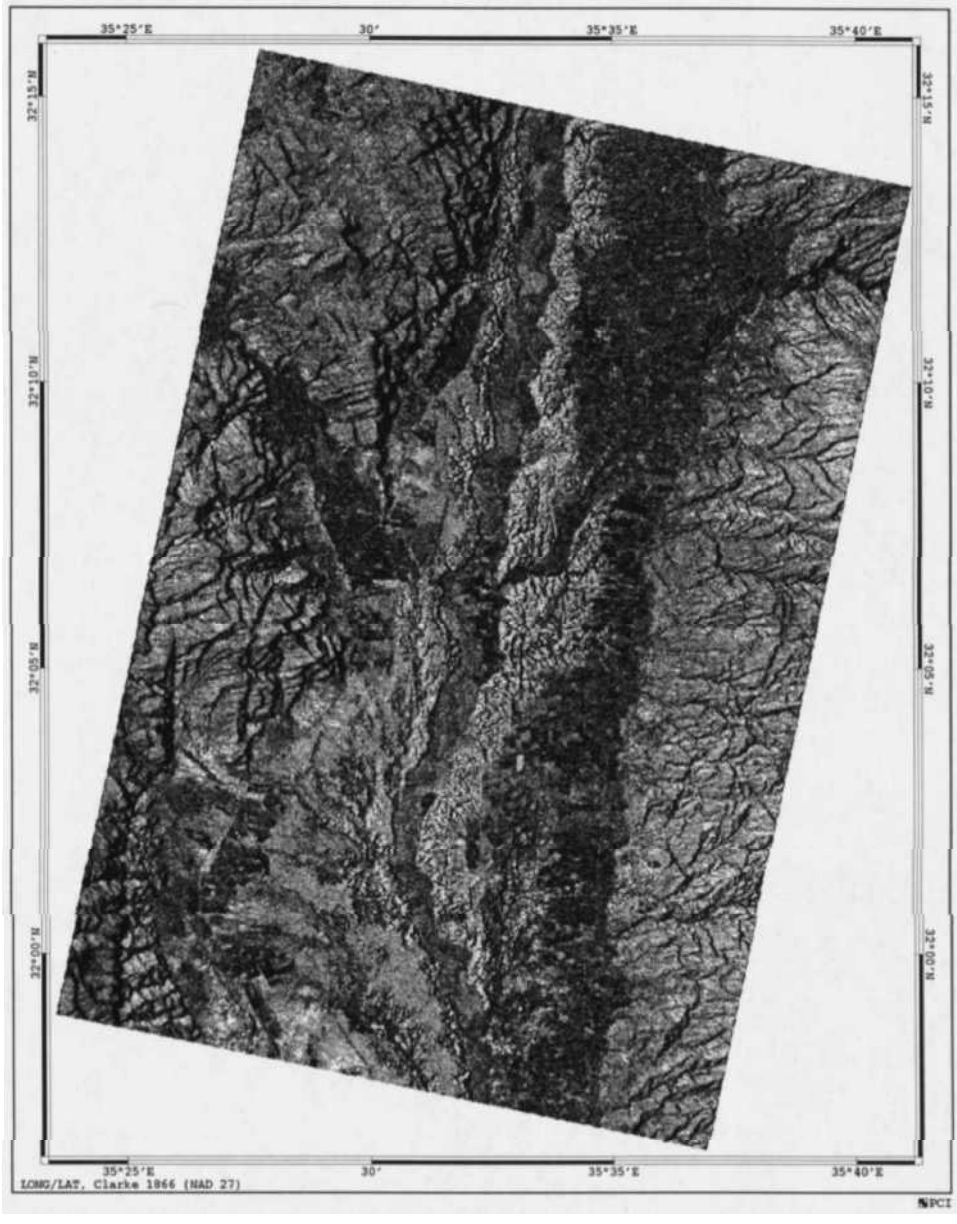

Figure 5. PCA1SC: Geocoded first principal component of the PCA between the SAR and coherence images.

(B2) which appears in bright tones in clear contrast with the dark-toned vegetated/agricultural alluvial area (B1), but also we have been able to distinguish five categories, which is a great improvement in comparison with the geological map of the area (figure 1) which shows only two units (Q and Q4) in this rift floor.

It is pertinent perhaps to review the probable reasons why the PCA1SC possesses the above attributes. It is a well known fact that the terrain factors which influence the intensity of radar returns include surface roughness, orientation, and dielectric

Figure 6. Landsat-TM false-colour composite (with bands 2, 3, and 4 assigned to blue, green, and red colours respectively).

constant (which itself increases with the moisture content of the material). These characteristics concern the morphology of the surface (including its microtopography) as well as the landcover type and geometric properties. If we consider vegetation cover, for instance, its height, type (branching structure), and state (active or dry) reflects in the image intensity. On the other hand, the main terrain factor influencing the intensity of coherence images consists basically of changes in the surface during the time interval separating the acquisition of the two images constituting the

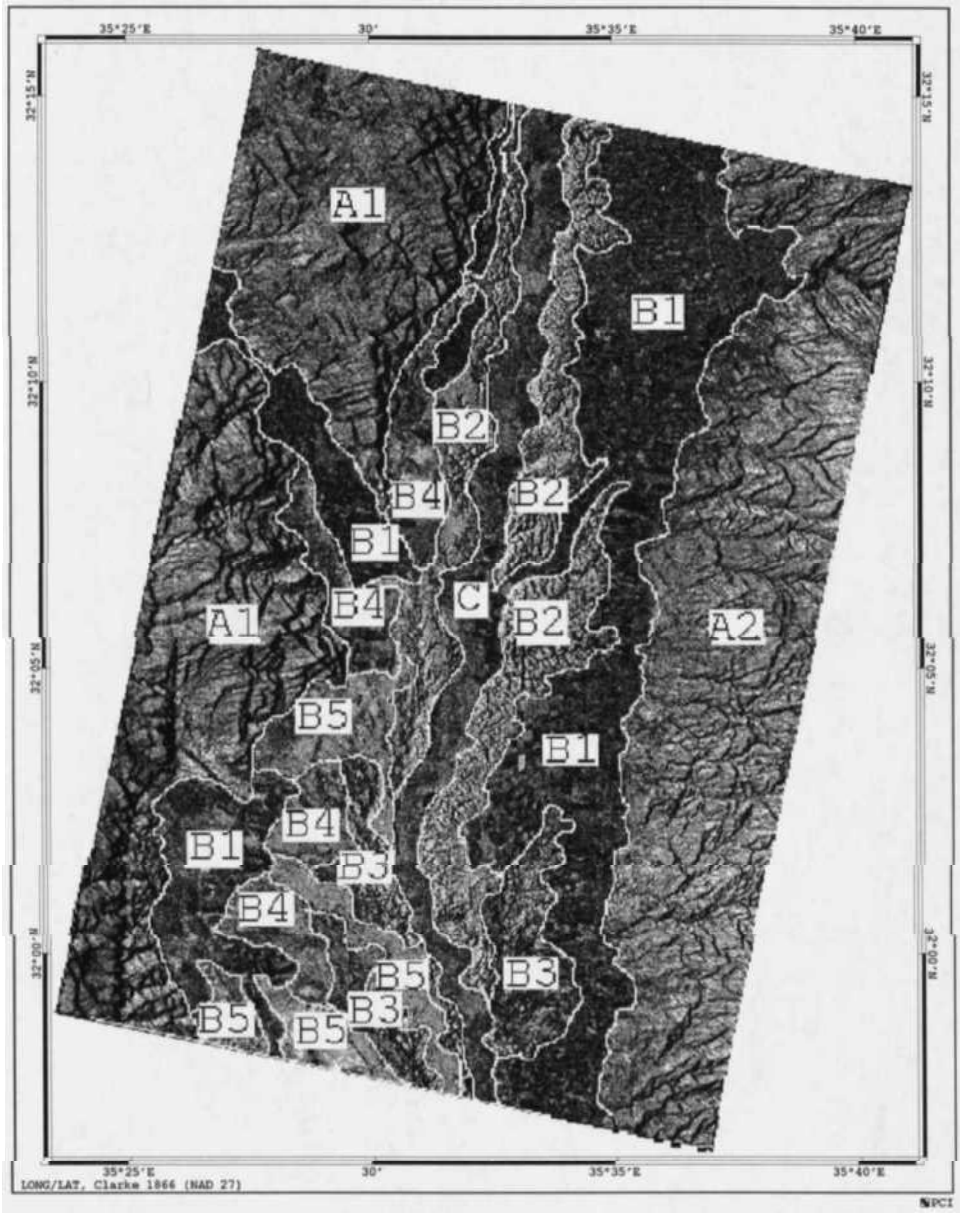

Figure 7. Lithologic interpretation of the PCA1SC shown in figure 5: A1: Upper Cretaceous to Eocene limestone, dolomite, marl, chalk, and chert forming the western Rift Valley shoulder. A2: Lower to Upper Cretaceous sandstone, limestone, dolomite, and marl forming the eastern Rift Valley shoulder. B1: Quaternary Terra Rosa soils overlying Lisan Formation clastic and lacustrine valley fill sediments. B2: Pliocene to Quaternary Lisan Formation—forming badlands. B3: Pliocene to Quaternary Lisan and Damya Formations mixed with soils—partly badlands. B4: Quaternary to recent Terra Rosa soils with relics of Lisan formation. B5: Quaternary Lisan and Damya formations, clastics with some soil component. C: Recent to present-day Jordan river flood plain of fluvial and alluvial sediments.

interferometric pair. Therefore, the PCA1SC integrates information related to surface roughness, orientation, cover, moisture content, and change factor over time; all of which are indicators of lithologic differences. By comparison, visible/infrared systems, such as Landsat, sense mainly the spectral characteristics (colours, so to speak) of the surface and surface cover. Thus, for instance, the expression of vegetation cover is dominated mostly by its greenness (i.e., chlorophyll content), while its geometric properties have little or no influence. Although, visible/infrared images in certain cases express lithologic differences quite well, the advantage of the PCA1SC emanates from the fact that it uses a different but larger set of variables. Moreover, unlike the Landsat-TM image, the PCA1SC is not cluttered with spectral details, such as roads and other features, which sometimes hinder geological interpretation.

In addition to the above stated advantages, the PCA1SC also appears to be potentially well disposed (better than the SAR and coherence images considered individually) to such digital techniques as textural analysis, segmentation, and feature extraction. We will be working along these lines shortly.

6. Conclusion

Valuable results have been achieved by applying such a simple process as Principal Components Analysis to datasets of such modest visual quality as coherence and SAR images. This is inspite of the fact that coherence images have often been treated with little importance, and that Principal Components Analysis is one of the simplest and most common image processing techniques available. Thus, we have been able to show that coherence images harbour a great deal of potential for improving the quality of SAR images for a number of useful (notably geological) applications. However, the main inconvenience of this process is that coherence images cannot be obtained without going through the rigours of selecting and procuring interferometric pairs (meeting strict baseline, time interval, and view angle requirements), and performing interferometry. Nevertheless, the main attraction of the result of this work lies in the fact that it symbolizes a simple approach to recycling coherence images which have until recently been regarded almost as a waste by-product of interferometry.

It is very encouraging that SAR and its two main interferometric products (interferogram and coherence) can be of vital use. It has been a well known fact that amplitude SAR images provide a variety of information related to surface characteristics, interferograms provide elevation and ground displacement information, and coherence images contain surface change information. Based on the result of this work, it is now obvious that the synergy of the coherence and SAR images can enhance the expression of lithologic differences. The main significance of this is that areas where the acquisition of visible/infrared images is problematic, such as cloud covered tropical areas, can now be mapped both topographically and geologically using SAR imagery and limited supplementary data. We are therefore approaching an era of fewer limitations on mapping from space (globally speaking), thanks to information obtainable from SAR.

Acknowledgments

This work was jointly sponsored by the Israeli Ministry of Science and Arts (through the Israel Space Agency, ISA) and the French Space Agency (CNES). The ISAR software used for interferometry was provided by the European Space Agency (ESA). We are very grateful to them.

References

Askne, J., and Hagberg, J. O., 1993, Potential of interferometric SAR for classification of land surfaces. *Proceedings of the International Geoscience and Remote Sensing Symposium (IGARSS'93), Tokyo, Japan, 18–21 August 1993* (Piscataway: I.E.E.E.), pp. 985–987.

Bamler, R., and Just D., 1993, Phase statistics and decorrelation in SAR interferograms. *Proceedings of the International Geoscience and Remote Sensing Symposium (IGARSS'93) Tokyo, Japan, 18–21 August 1993* (Piscataway: I.E.E.E.), pp. 980–984.

Bartov, Y., and Arkin, Y., 1979, *The Geological Photomap of Israel on a scale of 1 : 500 000* (Tel Aviv: Israel Survey).

Beauchemin, M., Thomson, K. P. B., and Edwards, G., 1996, Edge detection and speckle adaptive filtering for SAR images based on a second-order textural measure. *International Journal of Remote Sensing*, **17,** 1751–1759.

Coulson, S. N., and Solaas, G. A., 1993, SAR interferometry with ERS-1. In *CNES From Optics to Radar, SPOT and ERS Applications* (Toulouse: Cépaduès-Editions), pp. 457–472.

D'Iorio, M. A., Brisco, B. G., Budkewitsch, P. A., Geudtner, D., Vachon, P. W., and Wolfe, J., 1996, Geological and morphological control on ERS-1 SAR coherence images of Bathurst Island. *Proceedings of the 26th International Symposium on Remote Sensing of Environment and the 18th Annual Symposium of the Canadian Remote Sensing Society, Vancouver, BC, Canada, 25–29 March 1996* (Ottawa: Canadian Remote Sensing Society), pp. 107–111.

Gens, R., and Van Genderen, J. L., 1996, SAR interferometry—issues, techniques, applications. *International Journal of Remote Sensing*, **17,** 1803–1835.

Goldstein, R. M., Barnett, T. P., and Zebker, H. A., 1989, Remote sensing of ocean currents. *Science*, **246,** 1282–1285.

Goldstein, R. M., Engelhardt, H., Kamb, B., and Frolich, R. M., 1993, Satellite radar interferometry for monitoring ice sheet motion: Application to an Antarctic ice stream. *Science*, **262,** 1525–1530.

Goldstein, R. M., and Zebker, H. A., 1987, Interferometric radar measurement of ocean surface currents. *Nature*, **328,** 707–709.

Hall, J. K., 1993, The GSI Digital Terrain Map (DTM) project completed. *Geological Survey of Israel Current Research*, **8,** 47–50.

Henebry, G. M., and Kux, H. J. H., 1995, Lacunarity as a texture measure for SAR imagery. *International Journal of Remote Sensing*, **16,** 565–571.

Lee, J. S., Hoppel, K. W., Mango, S. A., and Miller, A. R., 1994 a, Intensity and phase statistics of multilook polarimetric and interferometric SAR imagery. *I.E.E.E. Transactions on Geoscience and Remote Sensing*, **32,** 1017–1028.

Lee, J. S., Jurkevich, I., Dewaele, P., Wambacq, P., and Oosterlinck, A., 1994 b, Speckle filtering of synthetic aperture radar images: A review. *Remote Sensing Reviews*, **8,** 313–340.

Massonnet, D., and Rabaute, T., 1993, Radar interferometry: Limits and potential. *I.E.E.E. Transactions on Geoscience and Remote Sensing*, **31,** 455–464.

Massonnet, D., Rossi, M., Carmona, C., Adragna, F., Peltzer, G., Feigi, K., and Rabaute, T., 1993, The displacement field of the Landers earthquake mapped by radar interferometry. *Nature*, **364,** 138–142.

Mather, P. M., 1987, *Computer Processing of Remotely-Sensed Images: An Introduction* (Chichester: Wiley & Sons).

Rudant, J. P., Deroin, J. P., and Polidori, L., 1994, Multi-resolution analysis of radar images and its application to lithological and structural mapping; Larzac (southern France) test site. *International Journal of Remote Sensing*, **15,** 2451–2468.

Safa, F. and Flouzat, G., 1989, Speckle removal on radar imagery based on mathematical morphology. *Signal Processing*, **16,** 319–333.

Saint-Jean, R., Singhroy, V., and Khalifa, S. M., 1995, Geological interpretation of integrated SAR images in the Azraq area of Jordan. *Canadian Journal of Remote Sensing*, **21,** 511–517.

Schistad Solberg, A. H., Jain, A. K., and Taxt, T., 1994, Multisource classification of remotely sensed data: Fusion of Landsat-TM and SAR images. *I.E.E.E. Transactions on Geoscience and Remote Sensing*, **32,** 768–778.

Vachon, P. W., Geudtner, D., Gray, A. L., and Touzi, R., 1995, ERS-1 synthetic aperture radar repeat-pass interferometry studies: Implications for Radarsat. *Canadian Journal of Remote Sensing*, **21,** 441–454.

Wegmuller, U., Werner, C. L., Nuesch, D., and Borgeaud, M., 1995, Landsurface analysis using ERS-1 SAR interferometry. *ESA Bulletin*, **81,** 30–37.

Zebker, H. A., and Villasenor, J., 1992, Decorrelation in interferometric radar echoes. *I.E.E.E. Transactions on Geoscience and Remote Sensing*, **30,** 950–959.

Zebker, H. A., Werner, C. L., Rosen, P. A., and Hensley, S., 1994, Accuracy of topographic maps derived from ERS-1 interferometric radar. *I.E.E.E. Transactions on Geoscience and Remote Sensing*, **32,** 823–836.